Research Article | Vol. 11, No. 3 / 1 March 2021 / Optical Materials Express 913
Optical Materials EXPRESS

Sulfur-rich chalcogenide claddings for athermal and high-Q silicon microring resonators

PHILIPPE JEAN,[1,2,4] ALEXANDRE DOUAUD,[1] TRISTAN THIBAULT,[3] SOPHIE LAROCHELLE,[1,2] YOUNÈS MESSADDEQ,[1,3] AND WEI SHI[1,2,5]

[1]*Centre d'Optique, Photonique et Laser (COPL), 2375 rue de la Terrasse, Université Laval, Québec, G1V 0A6, Canada*
[2]*Département de Génie Électrique et de Génie Informatique, Université Laval, 2325, rue de l'Université, Québec, G1V 0A6, Canada*
[3]*Département de Physique, de Génie Physique et d'Optique, Université Laval, 2325, rue de l'Université, Québec, G1V 0A6, Canada*
[4]*philippe.jean.4@ulaval.ca*
[5]*wei.shi@gel.ulaval.ca*

Abstract: Heterogeneous integration of materials with a negative thermo-optic coefficient is a simple and efficient way to compensate the strong detrimental thermal dependence of silicon-on-insulator devices. Yet, the list of materials that are both amenable for photonics fabrication and exhibit a negative TOC is very short and often requires sacrificing loss performance. In this work, we demonstrate that $As_{20}S_{80}$ chalcogenide glass thin-films can be used to compensate silicon thermal effects in microring resonators while retaining excellent loss figures. We present an experimental characterization of the glass thin-film and of fabricated hybrid microring resonators at telecommunication wavelengths. Nearly athermal operation is demonstrated for the TM polarization with an absolute minimum measured resonance shift of 5.25 pm K^{-1}, corresponding to a waveguide effective index thermal dependence of 4.28×10^{-6} RIU/K. We show that the thermal dependence can be controlled by changing the cladding thickness and a negative thermal dependence is obtained for the TM polarization. All configurations exhibit unprecedented low loss figures with a maximum measured intrinsic quality factor exceeding 3.9×10^5, corresponding to waveguide propagation loss of 1.37 dB cm^{-1}. A value of $-4.75(75)\times10^{-5}$ RIU/K is measured for the thermo-optic coefficient of $As_{20}S_{80}$ thin-films.

1. Introduction

The functionalities of silicon-on-insulator (SOI) can be greatly extended via the heterogeneous integration of advanced materials with complimentary properties and strengths. Hybrid integration then offers a simple solution to alleviate specific drawbacks of SOI that can hinder its development for certain applications. One of the major challenges of SOI is the high thermo-optic coefficient (*TOC*) of silicon ($TOC_{Si} = \frac{dn_{Si}}{dT} = 1.8\times10^{-4}$ K^{-1}) leading to unwanted thermal drift in wavelength selective components such as filters or resonators. In this case, cladding the silicon waveguides with a material that has a negative *TOC* can compensate the refractive index shift of silicon and lead to a reduced or even null thermally induced effective index shift. While multiple reports and demonstrations of athermal operation already exists in the literature [1–10], most of the research done on athermal silicon photonics is focused on waveguide design and their applications but rely on a handful of select materials that combine a negative *TOC* with interesting properties for heterogeneous integration, namely, some polymer composition or TiO_2. Demonstrations of new materials for thermal compensation are scarce at best [3]. Furthermore, the deposition of a top cladding using these materials is generally accompanied by large additional losses

#421814 https://doi.org/10.1364/OME.421814
Journal © 2021 Received 4 Feb 2021; revised 19 Feb 2021; accepted 19 Feb 2021; published 26 Feb 2021

Optical Materials EXPRESS

[4,5]. Considering that loss management is equally important and challenging in SOI as thermal management, achieving athermal operation while keeping moderate loss is essential.

In this work, we propose $As_{20}S_{80}$ chalcogenide glass (ChG) as a negative *TOC* cladding material for SOI. We present experimental characterization of the glass thin-films, as $As_{20}S_{80}$ is seldom used and less known than its stoechiometric counterpart, As_2S_3. We then present results from the optical characterization of $As_{20}S_{80}$-on-Si microring resonators (MR) that show reduced thermally induced resonance shift with measured values as low as $\frac{\Delta\lambda_r}{\Delta T} = 13.95\,\text{pm}\,\text{K}^{-1}$ and $\frac{\Delta\lambda_r}{\Delta T} = 5.25\,\text{pm}\,\text{K}^{-1}$ for the TE and TM polarizations, respectively. In addition, we show that the use of $As_{20}S_{80}$ as the top cladding of the waveguide results in low propagation losses corresponding to intrinsic quality factors as high as 2.6×10^5 and 3.9×10^5 for the TE and TM polarizations, respectively. The article is concluded by putting the present work in context within the existing literature regarding athermal SOI.

Chalcogenide glasses have already been used in the context of silicon co-integration in efforts to leverage their excellent and unique optical properties [11]. For example, As_2S_3 silicon-slot waveguides were demonstrated as an attractive platform for χ_3 nonlinear photonics [12] while As_2S_3 waveguides are often combined with SOI circuits for their strong electrostrictive stimulated Brillouin scattering [13]. Additionally, As-S glasses have the rare property of being photosensitive in the near-infrared, allowing to use light for modification of the refractive index of the glass for resonance trimming or Bragg grating inscription [7,14–16].

2. Material and fabrication

The geometry of the hybrid ChG-on-Si waveguide is depicted in Fig. 1(a). The waveguide optical properties were simulated using a finite difference eigenmode solver (FDE). The simulated normalized electric field intensity mode profiles for the TM and TE polarizations in 220 nm thick and 300 nm wide waveguide are shown in Fig. 1(b) and (c), respectively. The distribution of the electric field indicates a strong delocalization of the mode from the silicon core and increased interaction with the top cladding. The ratio of the field that interacts with each material can be designed and optimized to control the effective index thermo-optic coefficient, as will be shown in later sections.

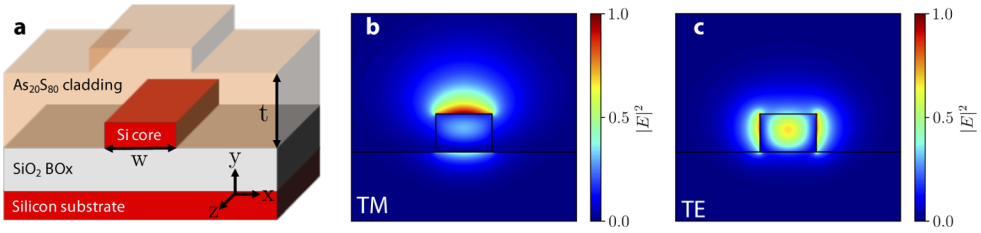

Fig. 1. (a) Schematic of the hybrid waveguide cross-section with core width w and cladding thickness t (not to scale). Simulated electric field intensity of the (b) TM and (c) TE polarization in a bent waveguide with $w = 300\,\text{nm}$ and $R = 100\,\mu\text{m}$ at $\lambda = 1550\,\text{nm}$.

2.1. Chip fabrication

The silicon chips were fabricated at Applied NanoTools through the SiEPICfab consortium using electron-beam lithography on standard 220 nm device thickness SOI wafers with a buried oxide (BOX) thickness of 2 µm [17]. The cladding was deposited at COPL following a method similar to that described in [18]. To assess the fabrication quality, the resulting hybrid devices were imaged using a scanning electron microscope (SEM) and focused ion beam (FIB) milling to expose the cross-sections. The SEM images are presented in Fig. 2. The next paragraphs provide details on the $As_{20}S_{80}$ thin-films that were not presented in [18].

Optical Materials EXPRESS

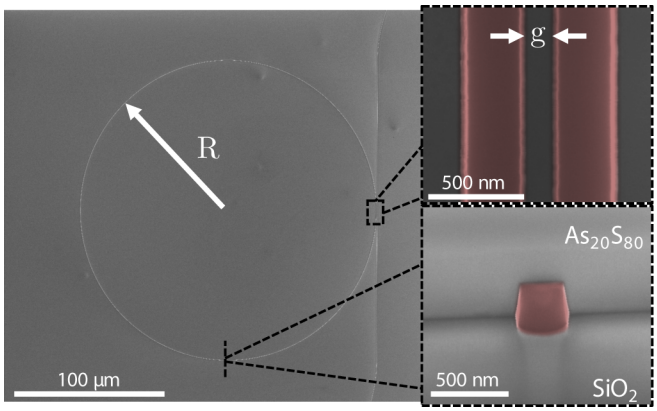

Fig. 2. Top view SEM image of a fabricated microring resonator with radius R before thin-film deposition. Inset on the right: close-up views of (top) the coupling region of the MR with a bus-ring gap g before deposition and (bottom) a FIB cross-section of the waveguide after deposition and thermal annealing. The silicon in the insets is false colored in red for better visibility.

First, chunks of the prepared $As_{20}S_{80}$ glass were laid in a molybdenum crucible for electron-beam-assisted depositions. The different thin-films were deposited onto rotating substrates to ensure homogeneous films, in an evaporation chamber evacuated to 5×10^{-7} Torr. An evaporation rate of 10 Å s^{-1} was chosen for its ideal results. The resulting measured thicknesses of the devices are summarized in Table 3. $As_{20}S_{80}$ was chosen as a cladding material for its interesting properties: low optical losses at 1550 nm and low glass transition temperature ($T_g \approx 100$ °C). Indeed, a low T_g allows us to perform thermal treatments on the thin-films at lower temperatures compared with As_2S_3 whose T_g is 100 °C higher [19]. Moreover, $As_{20}S_{80}$ being richer in sulphur than the well-known As_2S_3, it has an almost polymer-like behaviour toward temperature. Its sulphur-rich structural units confer the glass a less rigid overall structure and a capacity for reflow during thermal treatments much more proficient than As_2S_3 [18,20]. This property makes the material effective at filling in air gaps occurring during the deposition of thin-films onto chips with elaborate designs and provides a cladding that envelopes the silicon waveguide very well. Furthermore, an interesting property of $As_{20}S_{80}$ is its thermo-optical behavior: contrary to most oxide glasses and to As_2S_3, $As_{20}S_{80}$ possesses a negative thermo-optical coefficient (*TOC*, $\frac{dn}{dT}<0$). This behaviour can be explained by the greater polarisability of chalcogen atoms and their lower oscillator frequency [21]. Other materials, such as TiO_2 [8] or polymers [5], are also known to possess negative *TOC*, but unfortunately present high optical losses whereas $As_{20}S_{80}$ has low losses [18].

2.2. Glass thin-film characterization

A Raman spectroscopy analysis of the deposited $As_{20}S_{80}$ thin-film samples was performed to confirm the presence of sulphur-rich structural units. Figure 3(a) presents the resulting Raman spectrum and its deconvoluted curves. Bands located at 152, 218, 440, 466, 472, and 495 cm^{-1} confirm the existence of sulphur units: S_8 rings, and S_2 and S_n chains linking $AsS_{3/2}$ pyramidal units [20,22]. Furthermore, as-deposited thin-films were characterised by UV-Visible spectroscopy in order to determine the bandgap of $As_{20}S_{80}$. A material bandgap of $E_g = 2.68$ eV ($\lambda_g = 462$ nm) was extracted using Tauc plots of the thin-film, calculated from a transmission spectrum measured from 300 nm to 2500 nm (not presented here).

Thermal treatments carried out on fabricated chips and glass slides samples were performed using a Rapid Thermal Annealing oven (RTA), which uses an inert atmosphere composed of

Optical Materials EXPRESS

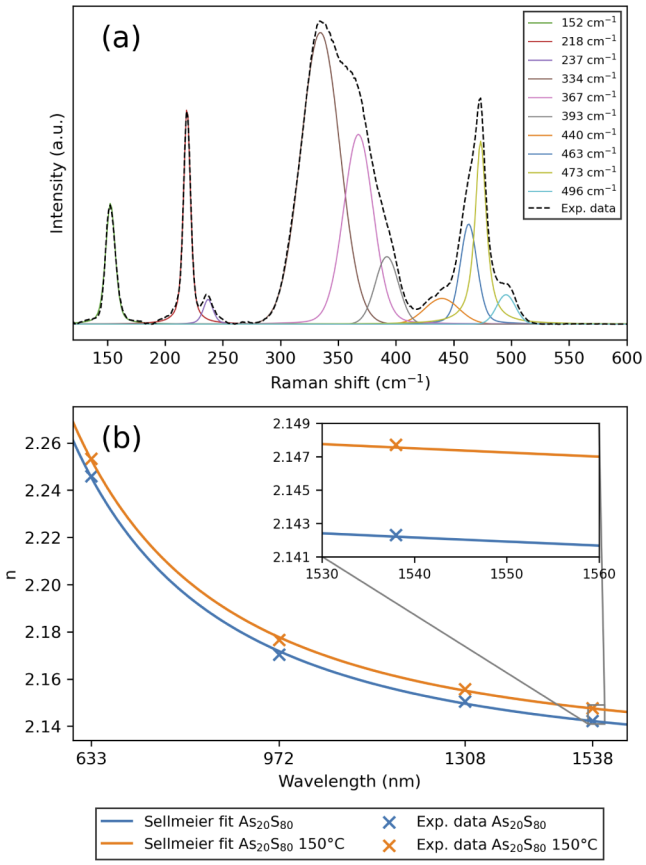

Fig. 3. (a) Raman spectrum of an $As_{20}S_{80}$ thin-film and its deconvolution curves, demonstrating the presence of sulphur-rich structural units. (b) Refractive indices of $As_{20}S_{80}$ before and after a thermal treatment at 150∘C for 2 min.

a mixture of argon and nitrogen (Ar/N_2). Samples were laid on a silicon wafer to ensure an optimal and clean annealing process. A heating rate of approximately 65 °C min^{-1} was used. In this study, a selected thermal treatment of 150 °C for 2 min is presented. Additionally, refractive index measurements were conducted using a prism-coupling technique at several wavelength. The resulting experimental data was then fitted using the Sellmeier equation [23]. Experimental and fitted data are presented in Fig. 3(b) and coefficients are summarised in Table 1. The slight increase in refractive index after annealing is explained by a molecular rearrangement leading to the densification of the glassy matrix, usually accompanied by a red-shift of the bandgap [24,25]. The prism-coupling experiment also provided the thin-film thickness. At this point, we note that our prism-coupling method provides accurate measurements at individual wavelength but the limited number of points limits the precision of the Sellmeier fit and therefore, will limit the precision of values interpolated from the fit and, more significantly, the material dispersion calculated from the fit. Therefore, other measurement methods, for example ellipsometry, should be considered in future works where accurate material dispersion is important.

Finally, to ensure the chemical composition stability of the thin-films against thermal treatments, an Energy-Dispersive X-ray spectroscopy (EDX) measurement was performed on a thin-film before and after annealing. Table 2 presents the elemental analysis of the as-deposited $As_{20}S_{80}$ thin-film before and after a thermal treatment of 150∘C for 2 min in an inert atmosphere (N_2/Ar).

Optical Materials EXPRESS

Table 1. Sellmeier coefficients used for the fitting of experimental data in Fig. 3(b).

$As_{20}S_{80}$ sample	Sellmeier coefficients		
	A	B	C [μm^2]
As deposited	1	3.509	5.292×10^{-2}
150∘C for 2 min	1	3.530	5.370×10^{-2}

The results being similar before and after thermal treatment (considering an instrumental incertitude of 1 %), it can be concluded that the thin-film's chemical composition is not altered during the annealing process.

Table 2. Elemental compositions measured by EDX using an acceleration of 20 kV, and analysis lines of K_α and L_α for As, and K_α for S.

$As_{20}S_{80}$ sample	Composition [at.%] (± 1 %)	
	As	S
As deposited	22.25	77.75
150∘C for 2 min	22.41	77.59

3. Optical characterization

Following characterization of the glass, thin-films were deposited directly onto the silicon chips for optical measurements, the devices tested are summarized in Table 3. The MRs were characterized using a laser sweep technique. Light was coupled to and from the chip using tapered optical fibers with a mode field diameter of 2.5 μm so that it is matched with the mode size of the on-chip inverse taper edge coupler. The chip was mounted on a thermoelectric cooler (TEC) to regulate the temperature. The measurements were first done with a fixed temperature of 20 °C. Following experimental data collection, the data was analyzed using in-house Python algorithms which provided with the resonant wavelengths λ_r, and transmittance at resonance T_0.

Table 3. Summary of the tested microring resonators

ID	w [nm]	g [nm]	t [nm]	R [μm]	Pol.
TE-640	300	200	640	100	TE
TE-950	300	200	950	100	TE
TM-640	300	250	640	100	TM
TM-950	300	250	950	100	TM

3.1. Group index

From the measured transmittance and resonant wavelengths, the group indices of the different geometries are calculated as $n_g = \frac{\lambda_{r,n}^2}{2\pi R|\lambda_{r,n-1}-\lambda_{r,n+1}|}$, the results are shown in Fig. 4. The void region in each curve of Fig. 4 corresponds to wavelengths where the coupling coefficient was too weak to observe the resonance, as discussed in Sect.3.2. Group indices calculated using FDE simulations are presented alongside the measured values in Fig. 4. The agreement is qualitatively good, with similar wavelength dependent behavior indicating normal dispersion in all cases. The discrepancies between simulated and measured group index are attributed to inaccuracies in the refractive index and film thickness measurement that were used in the simulation. The refractive index and dispersion at 1550 nm are obtained from the first order Sellmeier fit, which allow for

Optical Materials EXPRESS

some error since the number of points in the fit is rather low (4). The difference is stronger for the TM polarization, which is to be expected since the TM mode interacts more with the cladding material and is therefore more susceptible to variations in its properties.

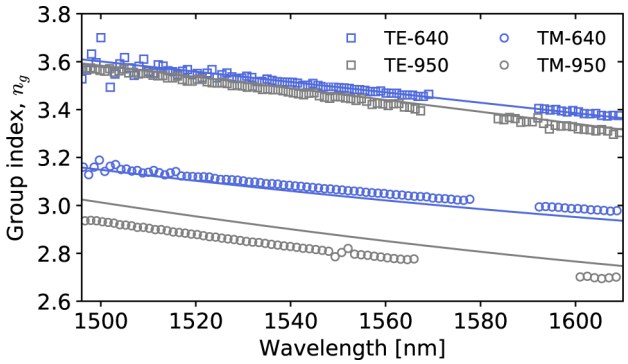

Fig. 4. Measured group index (markers) for the four tested MR alongside simulated group index (full lines).

3.2. Quality-factor

From the measured transmittance, each individual resonance was fitted to a Lorentzian function to extract the linewidth $\delta\lambda_{3dB}$ and the corresponding loaded quality factor $Q = \frac{\lambda_r}{\delta\lambda_{3dB}}$, the results are presented in Fig. 5(a) and (b). The spectral dependence of Q is mainly due to the varying coupling strength $|\kappa|$ in the microring, resulting in a periodic wavelength dependence. This periodicity of the coupling strength can be understood by the fact that the large radius R and the low-confinement with a small gap g result in a strong coupling coefficient and a finite coupling length [26]. The evolution of $|\kappa|$ is annotated on Fig. 5(a) and (b) alongside the approximate zones where the MRs operate in overcoupled and undercoupled regime. The different coupling regimes were inferred from the loaded quality factor and the extinction ratio of the resonances [27]. The regions where $|\kappa| \sim 0$ are void of resonances and correspond with the blank regions in Fig. 5. In general and over the spectral range considered, the shorter wavelengths displayed stronger coupling and overcoupled behavior. The strongly overcoupled and broad resonances were difficult to analyze correctly for our Python algorithm, which resulted in inaccuracies on the λ_r values and resulted in some points slightly off the trend around 1500 nm for the TE-640 and TM-640 devices in Fig. 4, 6(c) and 7. Next, the intrinsic quality factor $Q_i = \frac{2Q}{1+\sqrt{T_0}}$ [28] of undercoupled resonances was calculated. The transmittance around the resonance exhibiting the highest Q_i for each polarization is shown in Fig. 5(b) and (d). The corresponding values are $Q_i = 2.6 \times 10^5$ for the TE mode and $Q_i = 3.9 \times 10^5$ for the TM mode. Using the group index measured previously, the waveguide propagation losses α can be extracted from Q_i. The resulting losses are $\alpha = 2.32\,\mathrm{dB\,cm^{-1}}$ and $\alpha = 1.37\,\mathrm{dB\,cm^{-1}}$ for the TE and TM modes, respectively. The best resonances were both measured in the device with $t = 640$ nm. Exciting the microresonators TM mode results in higher Q due to the lower interaction of the optical mode field with the roughness of the silicon waveguide etched sidewalls. This discrepancy between TE and TM propagation loss in narrow strip waveguides has been previously demonstrated theoretically [29].

3.3. Thermal behavior

Following the passive measurements presented in the last few paragraphs, the thermal dependence of the hybrid MR was studied by varying the TEC set temperature from 20 °C to 35 °C in steps of 3 °C and acquiring the transmittance using the same laser swept measurement previously

Optical Materials EXPRESS

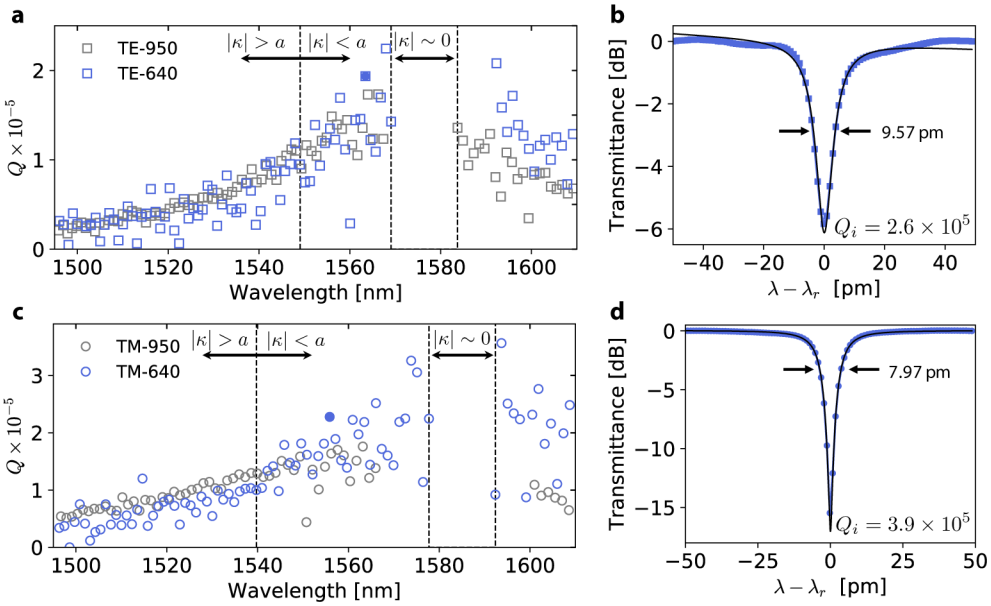

Fig. 5. Measured loaded quality factors for the MR for the (a) TE and (b) TM polarizations. The dashed vertical lines indicate the position where the TE-640 (TM-640) device operates in overcoupled ($|\kappa|>a$), undercoupled ($|\kappa|<a$) or uncoupled ($|\kappa| \sim 0$) regime, where a is the round-trip loss. (c) TE and (d) TM measured transmittance (markers) of single resonance with a Lorentzian fit (full line). The corresponding intrinsic quality factor are $Q_i = 2.6 \times 10^5$ and $Q_i = 3.9 \times 10^5$. The full marker in (a) and (b) indicate the location of the resonance shown in (c) and (d).

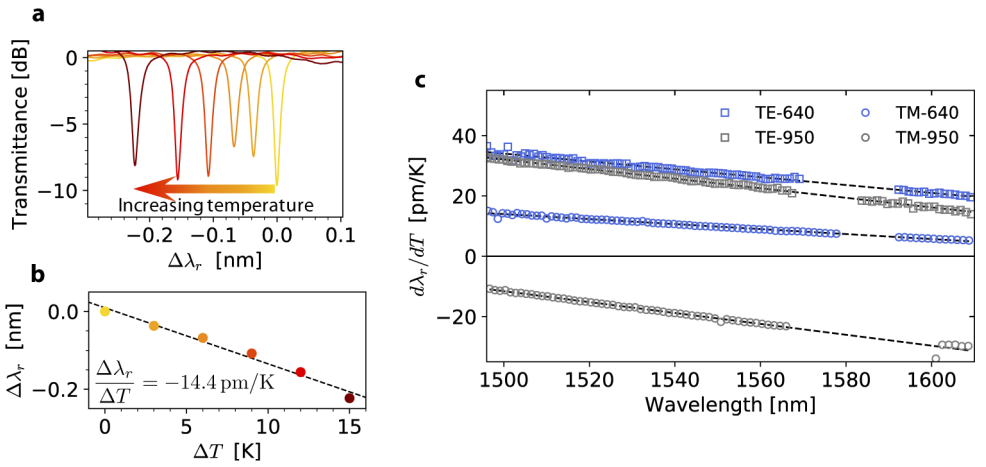

Fig. 6. (a) Transmittance of the TM-950 device around $\lambda = 1515$ nm as the temperature is increased and (b) measured (markers) resonant wavelength at the different temperatures alongside the linear fit (dashed black line) used for extracting the slope value of $\Delta\lambda_r/\Delta T = -14.4\,\mathrm{pm\,K^{-1}}$. (c) Measured resonance shift coefficient $d\lambda_r/dT$ (markers) for all the devices over the complete wavelength range alongside linear fit (dashed line) for visual aid.

described. For each resonance, the relation between the resonant wavelength shift and the temperature shift was fitted to a linear function. The slope of the function then directly provides

Optical Materials EXPRESS

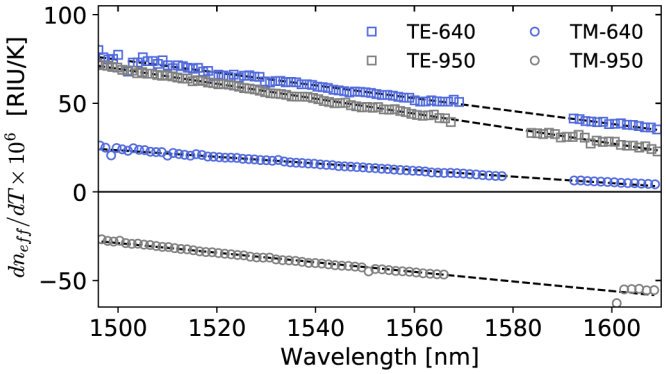

Fig. 7. Effective thermo-optic coefficient dn_{eff}/dT (markers) and linear fit (dashed line) used to calculate the dispersion (see text).

the wavelength shift per degree $d\lambda_r/dT \approx \Delta\lambda_r/\Delta T$. An example of this process of finding the resonance peaks and fitting a linear function to them is shown in Fig. 6(a) and (b). The lowest resonance shifts per degree measured are presented in Table 5 and the complete results over the wavelength span considered are shown in Fig. 6(c). Combining the data in Fig. 6(c) with the group index presented in Fig. 4, it is possible to calculate the value of the waveguide effective index thermo-optic coefficient $TOC_{eff} = dn_{eff}/dT$ using the relation [5,30]:

$$\frac{d\lambda_r}{dT} = \frac{\lambda_r}{n_g}\left(n_{eff}\alpha_{sub} + \frac{dn_{eff}}{dT}\right) \tag{1}$$

Where $\alpha_{sub} = 2.6\times10^{-6}\,\mathrm{K}^{-1}$ is the silicon substrate expansion coefficient [5] and the values of n_{eff} are taken from the simulations. The results are shown in Fig. 7. Every device has a reduced thermal dependence by at least an order of magnitude when compared with standard SiO_2 cladded SOI microring that exhibit values in the range of $dn_{eff}/dT \approx dn_{Si}/dT = 1.8\times10^{-4}$ at $\lambda = 1.55\,\mu\mathrm{m}$ [5]. All measurements also show a linear behavior with a monotonic decrease of dn_{eff}/dT at longer wavelength, which is expected as the mode becomes more and more delocalized in the negative *TOC* cladding. It is interesting to note that the spectral dependence of dn_{eff}/dT closely mimics that of the group index in Fig. 4, as expected since the group index away from absorption features is proportional to the effective index, which value is directly correlated to the interaction of the optical mode with the constituent materials of the waveguide. Both TM devices have the lowest thermal dependence with $dn_{eff}/dT = 4.28\times10^{-6}$ RIU/K and $dn_{eff}/dT = -26.8\times10^{-6}$ RIU/K for TM-640 and TM-950, respectively. Interestingly, the TM devices display a zero crossing between the two thicknesses considered, which indicates that true athermal operation ($dn_{eff}/dT = 0$ RIU/K) could be achieved by simply optimizing the cladding thickness t. We note that the net negative observed thermal dependence of TM-640 confirms that $As_{20}S_{80}$ has a negative *TOC*, as this behavior would not be possible otherwise. In contrast, the TE polarization resonance shift is less dependent of t and the minimum values measured are $dn_{eff}/dT = 22.8\times10^{-6}$ RIU/K and $dn_{eff}/dT = 35.3\times10^{-6}$ RIU/K for TE-950 and TE-640, respectively. The difference between TE and TM modes in this case is, of course, explained by their respective confinement factor Γ with the cladding and the high *TOC* silicon core. These results are in excellent accordance with simulations that suggest that longer wavelength and thicker cladding will increase the mode interaction with $As_{20}S_{80}$, resulting in reduced or negative resonance shift. Another relevant figure of merit is the *TOC* dispersion measured as the slope of dn_{eff}/dT vs wavelength. Real athermal operation using cladding *TOC* compensation is usually limited to a single wavelength point where dn_{eff}/dT crossover between positive and negative values. This behavior means that

Optical Materials EXPRESS

the dispersion of dn_{eff}/dT is relevant to increase the bandwidth of athermal operation. Here, the dispersion can be obtained directly from the slope of the linear fit shown in Fig. 7, the values are -3.62×10^{-7}, -4.21×10^{-7}, -1.86×10^{-7} and -2.71×10^{-7} RIU/K/nm for the TE-640, TE-950, TM-640 and TM-950 device, respectively. We can conclude that the TM mode would offer a wider bandwidth of nearly athermal operation around a potential athermal operation wavelength. The dispersion of dn_{eff}/dT is mainly attributed to the waveguide properties dispersion, mainly the confinement factor $\Gamma(\lambda)$.

3.4. Thermo-optic coefficient

Next, using simulated values of confinement factor Γ and known values for $dn_{Si}/dT = 1.8\times10^{-4}$ and $dn_{SiO_2}/dT = 8.4\times10^{-6}$ [5,30], it is possible to extract an approximated value for the *TOC* of $As_{20}S_{80}$ at 1550 nm using the relation [4]:

$$\frac{dn_{eff}}{dT} \approx \Gamma_{Si}\frac{dn_{Si}}{dT} + \Gamma_{SiO_2}\frac{dn_{SiO_2}}{dT} + \Gamma_{As_{20}S_{80}}\frac{dn_{As_{20}S_{80}}}{dT} \tag{2}$$

Where the confinement factor in material i is calculated as [31]:

$$\Gamma_i = \frac{n_g}{n_i}\frac{\iint_i \epsilon|\mathbf{E}|^2\,dx\,dy}{\iint_{\text{area}} \epsilon|\mathbf{E}|^2\,dx\,dy} \tag{3}$$

Equation (2) is an approximation neglecting higher-order thermal dependence and the variation of Γ with temperature and is only valid for moderate (not athermal) value of *TOC* and wavelength shifts of multiple pm K^{-1} [2]. Combining the experimental values of dn_{eff}/dT shown in Fig. 7 and the confinement factors obtained from simulations, it is possible to retrieve the material *TOC* of $As_{20}S_{80}$ with Eq. (2). By averaging the data from the four devices, we extract a value of $dn_{As_{20}S_{80}}/dT = -4.75(75)\times10^{-5}$ RIU/K. The value thus retrieved is compared with other negative *TOC* materials in Table 4. It's interesting to note that the value compares well with the one measured in bulk $As_{20}S_{80}$, even though discrepancies between the physical properties in the bulk and thin-film states could be expected [21].

Table 4. Thermo-optic coefficient of materials used for athermal integrated photonics

Material	$\frac{dn}{dT}$ [RIU/K]	Ref.
$As_{20}S_{80}$	$-4.75(75)\times10^{-5}$	This work
PSQ L152	-2.4×10^{-4}	[32]
SU-8	-1.1×10^{-4}	[33]
TiO_2	-2.15×10^{-4}	[8]
95% MAPTMS to 5% ZPO sol-gel	-1.52×10^{-4}	[3]

3.5. Athermal operation

For the sake of completeness, simulations of the bent waveguide ($R = 100\,\mu$m) were performed for both polarizations using the *TOC* obtained in the previous section at an operating wavelength $\lambda = 1550$ nm. The simulations provide the optical fields and the effective *TOC* is then calculated using Eq. (2). The results are summarized in Fig. 8(a) and (b) for the TE and TM mode, respectively. The general trend is as was inferred from the experimental measurements; the TM polarization is significantly more affected by the cladding thickness t while the TE polarization behavior is dictated almost exclusively by the silicon core width w. More insight on these simulation results is provided in Sect.4 alongside general design guidelines for achieving athermal operation using $As_{20}S_{80}$.

Optical Materials EXPRESS

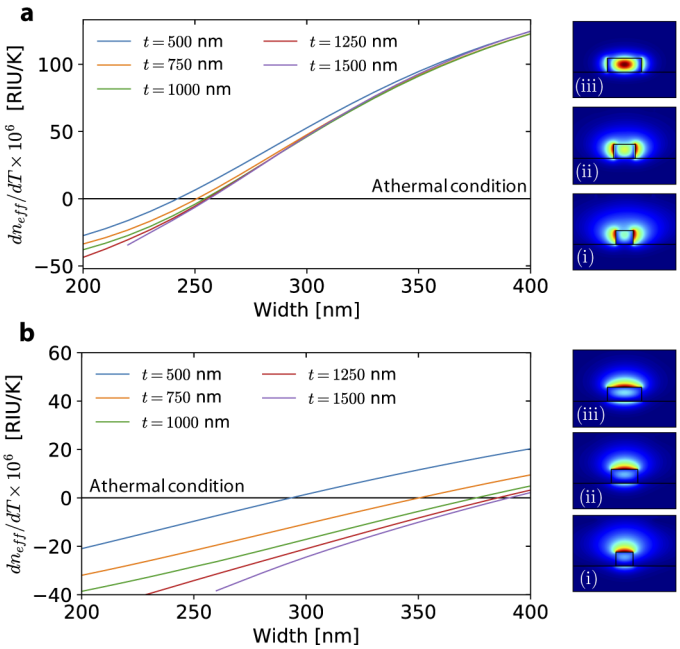

Fig. 8. Simulation of the effective thermo-optic coeffcient dn_{eff}/dT for various waveguide geometries in the (a) TE and (b) TM polarization. The insets show the electric field intensity for relevant geometries in (a): (i) w = 200 nm, t = 750 nm, (ii) w = 240 nm, t = 750 nm, (iii) w = 400 nm, t = 750 nm and (b): (i) w = 250 nm, t = 500 nm, (ii) w = 290 nm, t = 750 nm, (iii) w = 400 nm, t = 750 nm.

4. Discussion

The results achieved in this work are summarized and put into context within the existing literature in Table 5. With the exception of this work, the wavelengths are provided approximately for comparison only. We should also mention that the literature in Table 5 is chosen so that it can be directly compared with the main results of our work, that is, the authors reported nearly athermal wavelength shift and measured quality factor of their MR or waveguide propagation loss. Therefore, some valid demonstrations of athermal silicon operations are omitted but the conclusions that can be drawn from the data in Table 5 remain the same. Mainly, the use of $As_{20}S_{80}$ appears to solve a design quandary specific to low confinement structures in high index contrast waveguides like silicon. When the dominant source of loss is roughness from the silicon sidewalls, the use of narrowed waveguides to increase interaction with the low index cladding (polymer or SiO_2) results in additional losses due to more interaction with the sidewalls. Using a higher index cladding (n>2) provides a way around this problem by delocalizing and diluting the mode energy away from the sidewalls. Yet, only TiO_2 provides both a negative *TOC* and a sufficiently high index to achieve this effect but did not results in improved Q because of the large background losses in the TiO_2 layer [4]. Using $As_{20}S_{80}$ combines all the required properties (high index, low material loss and negative *TOC*) to solve this dilemma, as is reflected in the data of Table 5. Additionally, the losses measured in this work can be compared with standard SiO_2 cladded waveguides. The foundry provides loss standards of 1.5 dB cm^{-1} and 2.1 dB cm^{-1} for 500 nm wide waveguides for TE and TM polarization, respectively [34]. These values compares well with the loss demonstrated here, even though narrow waveguides (w = 300 nm) with low-index claddings would present high losses due to a combination of increased sidewall scattering and substrate leakage [35,36].

Optical Materials EXPRESS

Table 5. Comparison of reported athermal silicon microring resonators

Material	Design (Polarization)	$d\lambda_r/dT$[a] [pm · K^{-1}]	Q[b] ×10^5	Loss [dB · cm^{-1}]	λ[c] [nm]	Ref.
$As_{20}S_{80}$	Strip (TE)[d]	13.95	2.6	2.32	1610	This work
$As_{20}S_{80}$	Strip (TM)[e]	5.25	3.9	1.37	1610	This work
PSQ-LH	Strip (TE)	<5	-	50	1525	[5]
LFR-372	Strip (TE)	0.2	0.18	-	1550	[9]
Electro-optic polymer	Strip (TE)[f]	2.1	0.125	-	1550	[6]
As_2S_3 + Fluoropolymer[g]	(TM)	<1	0.15	-	1559	[7]
TiO_2	Strip (TE)	-30	-	16[h]	-	[10]
	Strip (TM)	40	-		1545	
TiO_2	Rib (TE)	-1.6	0.165	8	1548	[8]
TiO_2	Rib	<6	-	20	1300	[4]
95% MAPTMS to 5% ZPO sol-gel	Strip (TE)	-6.8	0.047	-	1550	[3]
	Strip (TM)	<1		-	1550	

[a]Minimum value measured, [b]Loaded and best reported, [c]Approximate values, [d]TE-950, [e]TM-640, [f]48 nm thick silicon, [g]As_2S_3 has a positive *TOC*, [h]Loss due to cladding layer only

We now draw attention to the quantitative performance achieved in this work in contrast with the literature. From observation of Table 5 and Fig. 6 and 7, it is obvious that the thermal dependence achieved here is not within the limit of what can be called athermal operation at telecommunication wavelength around 1550 nm, with the minimum shift of 5.25 pm K^{-1} occurring at the upper limit of the measured wavelength range and being nearly an order of magnitude larger in comparison with state-of-the-art demonstrations [7–9]. Nevertheless, we reiterate that the goal of this work is to study $As_{20}S_{80}$ as a candidate for future athermal design. Athermal operation could be achieved in the device shown in this work by operating slightly outside of the wavelength range measured. In fact, extrapolating the linear behavior shown in Fig. 7 provides athermal wavelengths of 1761 nm, 1702 nm, 1669 nm and 1436 nm for the TE-640, TE-950, TM-640 and TM-950, respectively.

In the case where athermal operation would be required at a specific wavelength within the C or L band for example, simple design guidelines can be applied and are confirmed in the simulations shown in Fig. 8. As such, optimizing the thickness offers a good control on the athermal behavior of the TM polarization, even for wider waveguides. This effect is limited and saturates as t becomes of the order of the wavelength, as can be seen from Fig. 8 when comparing the shift between the curves for thinner claddings (t = 500 – 750 nm) and the shift between the curves for thick claddings (t = 1250 – 1500 nm). Also for the TM polarization, changing the width of the waveguide has a weaker effect since the main electric field component is along the y-axis of the waveguide. The behavior is opposite for the TE polarization and the width serves to control the thermal behavior while the thickness has little effect. We note that athermal operation of the TE mode requires very narrow waveguides but are still well over the usual minimum feature size of UV lithography of around 150 nm. Combining a narrow waveguide and a thick cladding results in leaky modes for the TM polarization, which correspond to the lower limit of the curves t = 1250 nm and t = 1500 nm in Fig. 8. The simulations were done with R = 100 μm, for smaller radius, the bending loss will put a strict limit to the dimensions that can be used.

Other configurations also offer good control on the interaction between the optical fields and the cladding. For example, subwavelength grating waveguides (SWG) [37,38] can provide athermal operation when combined with a negative *TOC* cladding but generally suffer from

Optical Materials EXPRESS

higher scattering losses than strip waveguides [29,39]. They are nevertheless relevant in the context of athermal operation and should be studied in combination with $As_{20}S_{80}$ in future works.

Another important point to discuss regarding the use of $As_{20}S_{80}$ is its stability in extreme temperature environment. The keen reader will have realized that operation near the glass transition temperature of $As_{20}S_{80}$ ($T_g \approx 100\,°C$) is not advisable for the glass stability. Therefore, we believe the use of $As_{20}S_{80}$ is more relevant to compensate moderate temperature increases that can arise from optical power dissipation inside the silicon structures, from thermal crosstalk or from slight ambient temperature oscillations instead of use in extreme conditions or with metallic heaters. Of course, this is more or less speculative as rigorous experimentation will be required to establish temperature boundaries within which the $As_{20}S_{80}$ glass can be safely operated, which will be the subject of future works.

In summary, we demonstrated that $As_{20}S_{80}$ is a valid material to achieve thermal compensation in integrated photonics, specifically for the silicon-on-insulator platforms. The main advantage of using this glass in contrast with existing material solutions is the excellent loss performance which alleviates the usual need to compromise loss performance for thermal stability. This glass material is a crucial addition to a problematically short list of negative *TOC* materials for integrated photonics. Further research should focus on optimizing the waveguide dimensions to achieve exactly athermal operation at specified wavelengths and study the overall reliability and stability of using $As_{20}S_{80}$.

Funding. Natural Sciences and Engineering Research Council of Canada (STPGP 494358-16); Canada First Research Excellence Fund (Sentinel North).

Acknowledgments. The authors would like to thank Stéphan Gagnon and Wagner Correr for the SEM images.

Disclosures. The authors declare no conflicts of interest.

References

1. W. N. Ye, J. Michel, and L. C. Kimerling, "Athermal high-index-contrast waveguide design," IEEE Photonics Technol. Lett. **20**(11), 885–887 (2008).
2. V. Raghunathan, W. N. Ye, J. Hu, T. Izuhara, J. Michel, and L. Kimerling, "Athermal operation of silicon waveguides: spectral, second order and footprint dependencies," Opt. Express **18**(17), 17631–17639 (2010).
3. S. Namnabat, K.-J. Kim, A. Jones, R. Himmelhuber, C. T. DeRose, D. C. Trotter, A. L. Starbuck, A. Pomerene, A. L. Lentine, and R. A. Norwood, "Athermal silicon optical add-drop multiplexers based on thermo-optic coefficient tuning of sol-gel material," Opt. Express **25**(18), 21471–21482 (2017).
4. S. Feng, K. Shang, J. T. Bovington, R. Wu, B. Guan, K.-T. Cheng, J. E. Bowers, and S. J. B. Yoo, "Athermal silicon ring resonators clad with titanium dioxide for 1.3μm wavelength operation," Opt. Express **23**(20), 25653–25660 (2015).
5. J. Teng, P. Dumon, W. Bogaerts, H. Zhang, X. Jian, X. Han, M. Zhao, G. Morthier, and R. Baets, "Athermal silicon-on-insulator ring resonators by overlaying a polymer cladding on narrowed waveguides," Opt. Express **17**(17), 14627–14633 (2009).
6. F. Qiu, A. M. Spring, H. Miura, D. Maeda, M.-A. Ozawa, K. Odoi, and S. Yokoyama, "Athermal hybrid silicon/polymer ring resonator electro-optic modulator," ACS Photonics **3**(5), 780–783 (2016).
7. S. Grillanda, V. Raghunathan, V. Singh, F. Morichetti, J. Michel, L. Kimerling, A. Melloni, and A. Agarwal, "Post-fabrication trimming of athermal silicon waveguides," Opt. Lett. **38**(24), 5450–5453 (2013).
8. S. S. Djordjevic, K. Shang, B. Guan, S. T. S. Cheung, L. Liao, J. Basak, H.-F. Liu, and S. J. B. Yoo, "CMOS-compatible, athermal silicon ring modulators clad with titanium dioxide," Opt. Express **21**(12), 13958–13968 (2013).
9. M. M. Milošević, N. G. Emerson, F. Y. Gardes, X. Chen, A. A. D. T. Adikaari, and G. Z. Mashanovich, "Athermal waveguides for optical communication wavelengths," Opt. Lett. **36**(23), 4659–4661 (2011).
10. B. Guha, J. Cardenas, and M. Lipson, "Athermal silicon microring resonators with titanium oxide cladding," Opt. Express **21**(22), 26557–26563 (2013).
11. B. J. Eggleton, B. Luther-Davies, and K. Richardson, "Chalcogenide photonics," Nat. Photonics **5**(3), 141–148 (2011).
12. S. Serna, H. Lin, C. Alonso-Ramos, C. Lafforgue, X. L. Roux, K. A. Richardson, E. Cassan, N. Dubreuil, J. Hu, and L. Vivien, "Engineering third-order optical nonlinearities in hybrid chalcogenide-on-silicon platform," Opt. Lett. **44**(20), 5009–5012 (2019).
13. Y. Liu, A. Choudhary, G. Ren, K. Vu, B. Morrison, A. Casas-Bedoya, T. G. Nguyen, D.-Y. Choi, P. Ma, A. Mitchell, S. J. Madden, D. Marpaung, and B. J. Eggleton, "Integration of brillouin and passive circuits for enhanced radio-frequency photonic filtering," APL Photonics **4**(10), 106103 (2019).

Optical Materials EXPRESS

14. B. Shen, H. Lin, S. Sharif Azadeh, J. Nojic, M. Kang, F. Merget, K. A. Richardson, J. Hu, and J. Witzens, "Reconfigurable frequency-selective resonance splitting in chalcogenide microring resonators," ACS Photonics **7**(2), 499–511 (2020).
15. A. Canciamilla, F. Morichetti, S. Grillanda, P. Velha, M. Sorel, V. Singh, A. Agarwal, L. C. Kimerling, and A. Melloni, "Photo-induced trimming of chalcogenide-assisted silicon waveguides," Opt. Express **20**(14), 15807–15817 (2012).
16. J. Zhu, T. M. Horning, M. Zohrabi, W. Park, and J. T. Gopinath, "Photo-induced writing and erasing of gratings in As_2S_3 chalcogenide microresonators," Optica **7**(11), 1645–1648 (2020).
17. L. Chrostowski, H. Shoman, M. Hammood, H. Yun, J. Jhoja, E. Luan, S. Lin, A. Mistry, D. Witt, N. A. F. Jaeger, S. Shekhar, H. Jayatilleka, P. Jean, S. B.. Villers, J. Cauchon, W. Shi, C. Horvath, J. N. Westwood-Bachman, K. Setzer, M. Aktary, N. S. Patrick, R. J. Bojko, A. Khavasi, X. Wang, T. Ferreira de Lima, A. N. Tait, P. R. Prucnal, D. E. Hagan, D. Stevanovic, and A. P. Knights, "Silicon photonic circuit design using rapid prototyping foundry process design kits," IEEE J. Sel. Top. Quantum Electron. **25**(5), 1–26 (2019).
18. P. Jean, A. Douaud, V. Michaud-Belleau, S. H. Messaddeq, J. Genest, S. LaRochelle, Y. Messaddeq, and W. Shi, "Etchless chalcogenide microresonators monolithically coupled to silicon photonic waveguides," Opt. Lett. **45**(10), 2830–2833 (2020).
19. R. Blachnik and A. Hoppe, "Glass transition and specific heats in the systems P–S, P–Se, As–S and As–Se," J. Non-Cryst. Solids **34**(2), 191–201 (1979).
20. A. Douaud, S. H. Messaddeq, and Y. Messaddeq, "Microstructure formation in chalcogenide thin films assisted by thermal dewetting," J. Mater. Sci.: Mater. Electron. **28**(10), 6989–6999 (2017).
21. I. Shpak, I. Rosola, and O. I. Shpak, "Temperature dependence of the refractive index of glassy alloys of the As_xS_{100-x} system," J. Appl. Spectrosc. **84**(1), 140–143 (2017).
22. R. Golovchak, O. Shpotyuk, J. Mccloy, B. Riley, C. Windisch, S. Sundaram, A. Kovalskiy, and H. Jain, "Structural model of homogeneous As–S glasses derived from Raman spectroscopy and high-resolution XPS," Philos. Mag. **90**(34), 4489–4501 (2010).
23. Sellmeier, "Zur erklärung der abnormen farbenfolge im spectrum einiger substanzen," Ann. Phys. **219**(6), 272–282 (1871).
24. J. M. Laniel, J.-M. Ménard, K. Turcotte, A. Villeneuve, R. Vallée, C. Lopez, and K. A. Richardson, "Refractive index measurements of planar chalcogenide thin film," J. Non-Cryst. Solids **328**(1-3), 183–191 (2003).
25. C. Y. Yang, M. A. Paesler, and D. E. Sayers, "Measurement of local structural configurations associated with reversible photostructural changes in arsenic trisulfide films," Phys. Rev. B **36**(17), 9160–9167 (1987).
26. A. Yariv, "Coupled-mode theory for guided-wave optics," IEEE J. Quantum Electron. **9**(9), 919–933 (1973).
27. J. E. Heebner, V. Wongr, A. Schweinsberg, R. W. Boyd, and D. J. Jackson, "Optical transmission characteristics of fiber ring resonators," IEEE J. Quantum Electron. **40**(6), 726–730 (2004).
28. L. W. Luo, G. S. Wiederhecker, J. Cardenas, and M. Lipson, "High quality factor etchless silicon photonic ring resonators," Opt. Express **19**(7), 6284 (2011).
29. D. M. Kita, J. Michon, S. G. Johnson, and J. Hu, "Are slot and sub-wavelength grating waveguides better than strip waveguides for sensing?" Optica **5**(9), 1046–1054 (2018).
30. Y. Kokubun, N. Funato, and M. Takizawa, "Athermal waveguides for temperature-independent lightwave devices," IEEE Photonics Technol. Lett. **5**(11), 1297–1300 (1993).
31. J. T. Robinson, K. Preston, O. Painter, and M. Lipson, "First-principle derivation of gain in high-index-contrast waveguides," Opt. Express **16**(21), 16659–16669 (2008).
32. H. Zhang, J. Wang, L. Li, Y. Song, M. Zhao, and X. Jian, "Synthesis of liquid polysilisiquioxane resins and properties of cured films," Thin Solid Films **517**(2), 857–862 (2008).
33. P. Rabiei, W. H. Steier, C. Zhang, and L. R. Dalton, "Polymer micro-ring filters and modulators," J. Lightwave Technol. **20**(11), 1968–1975 (2002).
34. "Applied Nanotools Inc. - NanoSOI Fabrication Process," http://www.appliednt.com/nanosoi/. Accessed: 2021-02-19.
35. W. Bogaerts, R. Baets, P. Dumon, V. Wiaux, S. Beckx, D. Taillaert, B. Luyssaert, J. Van Campenhout, P. Bienstman, and D. Van Thourhout, "Nanophotonic waveguides in silicon-on-insulator fabricated with CMOS technology," J. Lightwave Technol. **23**(1), 401–412 (2005).
36. P. Dumon, W. Bogaerts, V. Wiaux, J. Wouters, S. Beckx, J. Van Campenhout, D. Taillaert, B. Luyssaert, P. Bienstman, D. Van Thourhout, and R. Baets, "Low-loss SOI photonic wires and ring resonators fabricated with deep UV lithography," IEEE Photonics Technol. Lett. **16**(5), 1328–1330 (2004).
37. J. H. Schmid, M. Ibrahim, P. Cheben, J. Lapointe, S. Janz, P. J. Bock, A. Densmore, B. Lamontagne, R. Ma, W. N. Ye, and D.-X. Xu, "Temperature-independent silicon subwavelength grating waveguides," Opt. Lett. **36**(11), 2110–2112 (2011).
38. M. Ibrahim, J. H. Schmid, A. Aleali, P. Cheben, J. Lapointe, S. Janz, P. J. Bock, A. Densmore, B. Lamontagne, R. Ma, D.-X. Xu, and W. N. Ye, "Athermal silicon waveguides with bridged subwavelength gratings for TE and TM polarizations," Opt. Express **20**(16), 18356–18361 (2012).
39. P. Jean, A. Gervais, S. LaRochelle, and W. Shi, "Slow light in subwavelength grating waveguides," IEEE J. Sel. Top. Quantum Electron. **26**(2), 1–8 (2020).